Solution structure of Ca^{2+}-free rat β-parvalbumin (oncomodulin)

MICHAEL T. HENZL[1] AND JOHN J. TANNER[1,2]

[1]Department of Biochemistry, University of Missouri-Columbia, Columbia, Missouri 65211, USA
[2]Department of Chemistry, University of Missouri-Columbia, Columbia, Missouri 65211, USA

(RECEIVED February 22, 2007; FINAL REVISION June 12, 2007; ACCEPTED June 13, 2007)

Abstract

Relative to other parvalbumin isoforms, the mammalian β-parvalbumin (oncomodulin) displays attenuated divalent ion affinity. High-resolution structural data for the Ca^{2+}-bound protein have provided little insight into the physical basis for this behavior, prompting an examination of the unliganded state. This article describes the solution structure and peptide backbone dynamics of Ca^{2+}-free rat β-parvalbumin (β-PV). Ca^{2+} removal evidently provokes significant structural alterations. Interaction between the D helix and the AB domain in the Ca^{2+}-bound protein is greatly diminished in the apo-form, permitting the D helix to straighten. There is also a significant reorganization of the hydrophobic core and a concomitant remodeling of the interface between the AB and CD-EF domains. These modifications perturb the orientation of the C and D helices, and the energetic penalty associated with their reversal could contribute to the low-affinity signature of the CD site. By contrast, Ca^{2+} removal causes a comparatively minor perturbation of the E and F helices, consistent with the more typical divalent ion affinity observed for the EF site. Ca^{2+}-free rat β-PV retains structural rigidity on the picosecond–nanosecond timescale. At 20°C, the majority of amide vectors show no evidence for motion on timescales above 20 ps, and the average order parameter for the entire molecule is 0.92.

Keywords: calcium-binding protein; EF-hand protein; parvalbumin; oncomodulin; NMR; structure; dynamics

Supplemental material: see www.proteinscience.org

The role of Ca^{2+} in eukaryotic signal transduction (Berridge et al. 2003; Berridge 2004, 2005) is facilitated by myriad Ca^{2+}-binding proteins. Many of these exhibit a metal ion-binding site consisting of a central binding loop and flanking helical segments. This motif is commonly known as the ''EF-hand'' because the arrangement of the loop and helices can be mimicked with the fingers of the right hand (Kretsinger 1980; Kawasaki and Kretsinger 1995; Celio et al. 1996).

Within the binding loop, the ligands to the bound ion are positioned at the vertices of an octahedron and, accordingly, are referenced by the axes of a Cartesian

Reprint requests to: Michael T. Henzl, Department of Biochemistry, 117 Schweitzer Hall, University of Missouri-Columbia, Columbia, MO 65211, USA; e-mail: henzlm@missouri.edu; fax: (573) 884-4812.

Abbreviations: ADR, ambiguous distance restraint; CD site, parvalbumin metal ion-binding site flanked by the C and D helices; CSI, chemical shift index; D_a, axial component of the molecular alignment tensor; $D_{\|}$, principal axis component of the molecular diffusion tensor; $D_{\perp}$, minor axis component of the molecular diffusion tensor in an axially symmetric system; DSS, sodium 2,2-dimethyl-2-silapentane-5-sulfonate; EDTA, ethylenediaminetetraacetic acid; EF site, parvalbumin metal ion-binding site flanked by the E and F helices; HEPES, 4-(2-hydroxyethyl)-1-piperazineethanesulfonic acid; HSQC, heteronuclear single-quantum coherence; Mes, 2-(N-morpholino)ethanesulfonic acid; NMR, nuclear magnetic resonance; NOE, nuclear Overhauser effect; NOESY, NOE spectroscopy; PV, parvalbumin; R, rhombic component of the molecular alignment tensor for partially aligned samples; R_1, longitudinal relaxation rate ($1/T_1$); R_2, transverse relaxation rate ($1/T_2$); RDC, residual dipolar coupling; RMSD, root mean square difference; S^2, generalized Lipari–Szabo order parameter; TALOS, torsion angle likelihood obtained from shifts and sequence similarity; τ_c, overall rotational correlation time; τ_e, internal correlation time; R_{ex}, rate constant for microsecond/millisecond motion resulting from chemical or conformational exchange.

Article and publication are at http://www.proteinscience.org/cgi/doi/10.1110/ps.072837307.

coordinate system (Kretsinger 1980; Strynadka and James 1989). The $-y$ ligand is a backbone carbonyl; $-z$ is a nearly invariant glutamate; and $-x$ is frequently water. The remaining ligands are side-chain oxygen atoms. Because the $-z$ glutamate binds Ca^{2+} in a bidentate manner, the coordination geometry is actually pentagonal bipyramidal. Despite the general similarity of their binding sites, EF-hand proteins exhibit broad variation in divalent ion-binding properties. The physical basis for the diverse behavior remains poorly understood.

Parvalbumins are small (12 kDa), vertebrate-specific EF-hand proteins (Heizmann and Kagi 1989; Pauls et al. 1996a). In fact, the crystal structure of carp parvalbumin (PV) established the EF-hand paradigm (Kretsinger and Nockolds 1973). The PV molecule includes six α-helices (A–F) organized into two domains—the AB domain (residues 1–38) and the CD-EF domain. The two metal ion-binding sites, the CD and EF sites, are named for the adjacent helices. In the Ca^{2+}-bound protein, they are related by an approximate twofold symmetry axis and are linked by a short fragment of antiparallel β structure.

The PV family includes α and β sublineages (Goodman and Pechere 1977; Moncrief et al. 1990), which can be distinguished on the basis of isoelectric point, C-terminal helix length, and several lineage-specific sequence assignments. Mammals express one α-PV and one β-PV (Fohr et al. 1993). The α-PV isoform serves as a cytoplasmic Ca^{2+} buffer in diverse tissue settings. The distribution of the β isoform, also called oncomodulin, is more limited. Until recently, the outer hair cell population in the organ of Corti was believed to be the sole site for expression in postnatal mammals (Henzl et al. 1997; Sakaguchi et al. 1998). However, Benowitz and colleagues have shown that oncomodulin is secreted by activated macrophages and functions as a potent nerve growth factor for retinal ganglion cells (Yin et al. 2006).

Despite 49% sequence identity with the rat α isoform (Berchtold and Means 1985; Gillen et al. 1987), rat β-PV exhibits substantially lower affinity for divalent ions (Hapak et al. 1989; Cox et al. 1990). In HEPES-buffered saline, at pH 7.4, the $\Delta\Delta G^{\circ\prime}$ for Ca^{2+} is 3.6 kcal/mol. When K^+ is the major solvent cation, this difference increases to 5.5 kcal/mol (Henzl et al. 2004b).

Although high-resolution structures are available for the Ca^{2+}-bound α- and β-parvalbumins from rat (Ahmed et al. 1993; McPhalen et al. 1994; Bottoms et al. 2004) and human (Babini et al. 2004; Baig et al. 2004), they offer little insight into the atypical metal ion-binding properties of the β isoform. It has been suggested that the unliganded state of the mammalian β-PV influences the divalent ion-binding signature (Henzl et al. 2004a). Reasoning that detailed structural information might help to clarify this issue, we have determined the solution structure and examined the peptide backbone dynamics of Ca^{2+}-free rat β-PV. Our findings are described herein.

Results

Resonance assignments

The 108-residue sequence of rat β-PV includes two proline residues (MacManus et al. 1983; Gillen et al. 1987). The protein is acidic (pI 3.85), with a predicted net charge of −14 at pH 6.0. Due, perhaps, to its highly anionic character, rat β-PV exhibits no tendency to self-associate at the concentrations employed for NMR spectroscopy, in either the Ca^{2+}-free or -bound forms (Henzl et al. 2002). At 20°C, the apo-protein exhibits a well-resolved ^{1}H-^{15}N HSQC spectrum (Fig. 1), which differs perceptibly from that collected on the Ca^{2+}-loaded protein under the same conditions (Supplemental Fig. S1). Except for G56, which is weak, all of the expected 105 amide signals are readily discernible. The following pairs of resonances are highly overlapped: I5/Y65, I11/A12, D22/F49, D45/F66, D53/R75, and Q42/S108.

Complete backbone assignments (H^N, N, C^α, H^α, C^β, C′) were made using a suite of three-dimensional, triple-resonance experiments. Representative strip plots for residues 31–41 are displayed in Supplemental Figure S2. Side-chain aliphatic carbon assignments were likewise complete, neglecting the carboxylate (Asp, Glu), carboxamide (Asn, Gln), and guanidinium (Arg) carbon atoms. Side-chain proton assignments (aliphatic and aromatic) were 96% complete, lacking chemical shifts for the H^ζ atoms of the 8 Phe residues; $H^{\delta 2}$, $H^{\varepsilon 1}$, and $H^{\varepsilon 2}$ of His-107 and $H^{\eta 11}$, $H^{\eta 12}$, $H^{\eta 21}$, and $H^{\eta 22}$ of Arg-48 and Arg-75. Assignments were made for just half of the C^δ-and C^ε-ring carbons of Phe and Tyr, and the C^γ and C^ζ carbons were left unassigned.

The tabulated chemical shifts served as input for CSI and TALOS. The former returned ϕ and ψ estimates for 62 residues. The latter provided ''good'' ϕ,ψ predictions for 47 residues. CSI identified the following helical regions—residues 8–17, 27–36, 40–49, 61–67, 79–88, and 99–105.

Solution structure of Ca^{2+}-free rat β-parvalbumin

The tertiary structure of Ca^{2+}-free rat β-PV was calculated with distance, dihedral, and RDC restraints (Table 1, Supplemental Fig. S3). Figure 2 displays an ensemble of the 20 lowest-energy conformers. Relative to the ensemble average, the RMSD is 0.39 Å for the backbone atoms (C^β, C^α, C′, O, and N) and 0.99 Å for all heavy atoms. According to PROCHECK, 97% of the

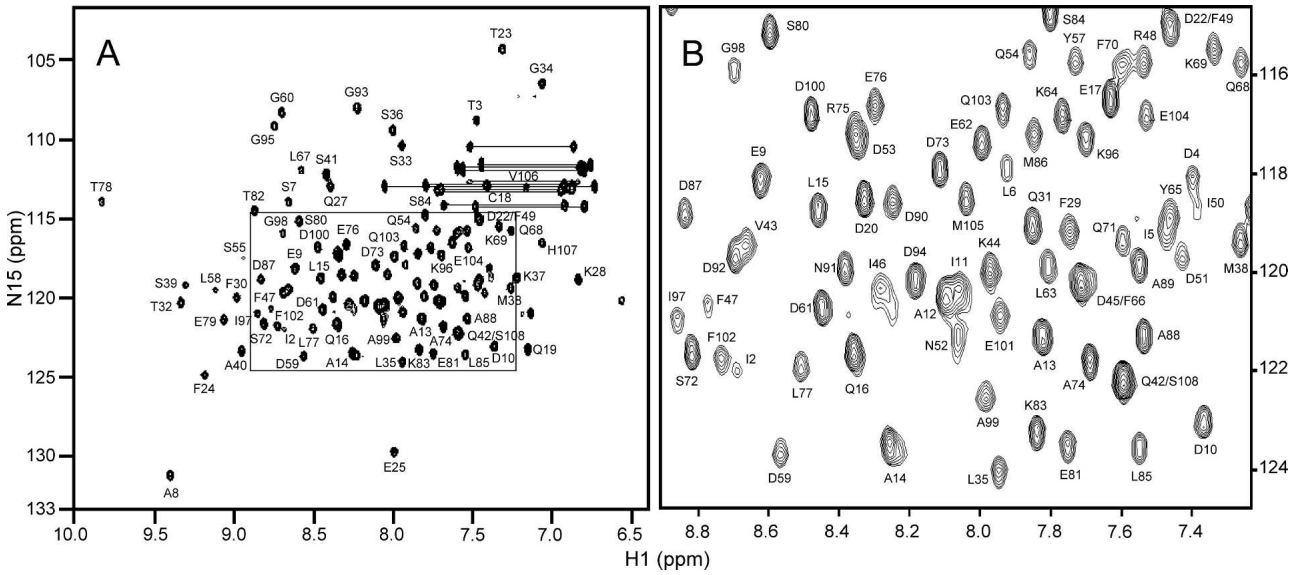

Figure 1. (*A*) ^{1}H-^{15}N HSQC spectrum of Ca^{2+}-free rat β-PV in 0.15 M NaCl, 0.01 M Mes (pH 6.0), at 20°C. (*B*) Expanded view of the crowded central region.

observed ϕ,ψ combinations reside in allowed regions of the Ramachandran plot. The structures exhibit good agreement with the experimental restraints. On average, there are just 3.7 NOE violations in excess of 0.5 Å. Fewer than 7% of the CSI and TALOS restraints are violated by more than 5°, and the RMSD between the calculated and observed RDC values is 0.77 Hz. Table 1 summarizes the structural quality statistics for the ensemble.

Comparison of the Ca^{2+}-bound and Ca^{2+}-free β-PV structures

The representative Ca^{2+}-free structure is shown superimposed on the crystal structure of the Ca^{2+}-bound protein (PDB 1RR0) in Figure 3. Removal of Ca^{2+} evidently provokes significant structural alterations. Although the relative positions of helices A, B, and F remain largely unchanged in the apo-protein, the C, D, and E helices have undergone substantial reorientation. There has also been some reshuffling of the side chains comprising the hydrophobic core, which results in modification of the interface between the AB and CD-EF domains.

Figure 4A displays the changes in the interhelical contact area that accompany Ca^{2+} removal. Helix D exhibits sharply reduced contact with the A and B helices and significantly reduced contact with helix F. Conversely, increased interaction is observed between the BC, BE, and CE helix pairs. The F helix displays perceptibly greater association with helices C and E and modestly diminished association with helix B. The interhelical contact values for the apo- and Ca^{2+}-loaded forms are listed in Supplemental Table S1.

Figure 4B offers further insight into the extent of the structural rearrangement, displaying alterations in pairwise residue contacts. For clarity, only the more prominent changes have been displayed. Cyan and blue represent decreases in the contact surface area that accompany Ca^{2+} removal; orange and red represent increased interresidue contact. Three regions of the graph have been emphasized. The central ellipse highlights interactions between the AB and CD-EF domains that are significantly diminished in the apo-protein. The bounded region near the lower left corner underscores interactions within the AB domain that increase with Ca^{2+} removal. The small ellipse near the right edge corresponds to altered pairwise interactions at the interface of the CD and EF metal ion-binding loops.

Total contact between the AB and CD-EF domains, 1959 Å^2 in the crystal structure, is essentially unchanged in the apo-protein (1987 ± 60 Å^2). However, the agreement of these two values is misleading. In fact, the apolar interdomain contact area has decreased from 1501 Å^2 to 1363 ± 38 Å^2 with removal of Ca^{2+}, a reduction of $9.2\% \pm 2.5\%$. This decrease is masked by a compensatory change in polar surface area, the latter occurring almost entirely at the periphery of the protein.

F70 evidently occupies a strategic position in the Ca^{2+}-bound protein, anchoring the C terminus of helix D to the AB domain. This interdomain association, which requires substantial bending of the D helix, is apparently absent in the Ca^{2+}-free state. As shown in Figures 3 and 5, F70 and F66 have both withdrawn from the hydrophobic core. Their displacement is accompanied by straightening of helix D. Relative to its position in the Ca^{2+}-bound protein,

Table 1. *List of restraints and statistical analysis for the apo-rat β-PV solution structure*

Number of experimental restraints	
Total NOEs	2895
Unambiguous	2209
Ambiguous	686
Intraresidue	1278
Sequential	791
Medium-range ($1 < \|i - j\| \leq 4$)	864
Long-range ($\|i - j\| > 4$)	1193
TALOS	94
CSI	124
Karplus (HNHA)	70
Residual dipolar couplings	93
Restraint violations (ensemble averages)	
NOE restraints (>0.5Å)	3.7 ± 1.6
Dihedral restraints (>5°)	15.2 ± 1.8
$^3J_{HNHA}$(>1 Hz)	29.9 ± 2.1
Dipolar coupling (>1 Hz)	17.0 ± 2.4
RMSD from experimental restraints	
NOE restraints (Å)	0.074 ± 0.010
Dihedral restraints (°)	3.71 ± 0.17
$^3J_{HNHA}$ (Hz)	1.51 ± 0.07
Dipolar coupling (Hz)	0.77 ± 0.05
RMSD from idealized covalent geometry	
Bonds (Å)	0.0079 ± 0.0002
Angles (°)	0.98 ± 0.02
Improper angles (°)	1.24 ± 0.04
Mean energies (kcal mol^{-1})	
NOE	570 ± 58
Bond	102 ± 6
Angle	437 ± 20
Cdih	185 ± 17
Coup	160 ± 15
SANI	56.8 ± 7.9
Coordinate RMSD from average structure (Å)	
Backbone (C^β, C^α,C′,O, N)	0.39
All heavy atoms	0.99
Ramachandran plot (ensemble average)	
Most favored regions (%)	72.5
Allowed regions (%)	19.5
Generously allowed (%)	5.5
Disallowed (%)	2.6

the α-carbon of F70 is displaced by 9 Å. As shown in Figure 4B, F70 experiences loss of contact with L6, I11, L15, F29, and L35. Significantly diminished contact is also observed between the AB domain and residues 66, 67, and 75.

Interestingly, residues 66, 67, 68, 70, and 71 display increased contact with residues at the N terminus. The backbone atoms of S1 and I2 are not observed in 3D NMR spectra of Ca^{2+}-bound rat β-PV, presumably due to exchange broadening. The putative interaction between the N terminus and the D/E loop in the apo-protein may limit mobility sufficiently to permit their detection.

In contrast to F66 and F70, F49 assumes a more interior position in the apo-protein. The side chains of I46, I50, and L85 likewise exhibit significant displacements. Apparently, Ca^{2+} removal provokes substantial reorganization of the hydrophobic core. As a result, the AB/CD-EF interface undergoes substantial remodeling. In the Ca^{2+}-bound protein, L6, I11, L15, F24, F29, and L35 participate in numerous interdomain contacts. In the apo-protein, however, the hydrophobic interactions involving these side chains are primarily intradomain (Fig. 6).

Although rat β-PV does not spontaneously form disulfide-linked dimers, either in the presence or absence of Ca^{2+}, dimer formation can be induced by treatment with Cu^{2+} (Clayshulte et al. 1990). Interestingly, the apo-protein undergoes Cu^{2+}-facilitated dimerization far more rapidly than the Ca^{2+}-bound form. This finding suggests that accessibility of the C18 sulfhydryl increases upon removal of Ca^{2+}. Consistent with the observed reactivity, solvent exposure of the sulfhydryl group is increased in the apo-protein (data not shown).

In the Ca^{2+}-bound state, paired EF-hand motifs are related by a pseudo-twofold symmetry axis and are physically linked by a short segment of antiparallel β structure. In rat β-PV, the fragment of β structure joining the CD and EF loops is created by hydrogen bonds between the main-chain carbonyl and amide groups of L58 and I97. With Ca^{2+} removal, these bonds are broken, and the orientations of the binding loops change perceptibly. The accompanying alterations in pairwise interaction are displayed in Figure 4B, bounded by the ellipse labeled β; whereas Y57 and D59 exhibit diminished contact with residues K96 and I97, residues 50–54 display increased interaction with 96 and 97.

Compared to the structural changes observed in the CD site (residues 41–70), the perturbations in the EF site (residues 81–108) provoked by Ca^{2+} removal appear fairly modest. As Figure 3 illustrates, the placement of the F helix is essentially unchanged. And although the E helix has moved, the displacement has evidently occurred with virtually no rotation of the helix or reorientation of its axis.

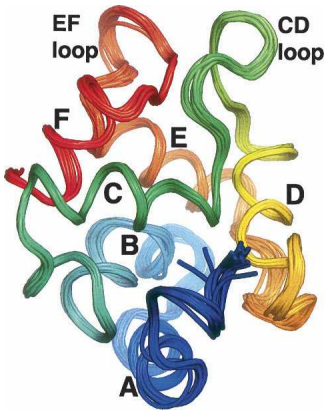

Figure 2. Solution structure of Ca^{2+}-free rat β-PV. An ensemble of the 20 lowest energy structures determined with ARIA-CNS. This figure and Figures 3, 5, and 6 were produced with PyMOL (DeLano 2002).

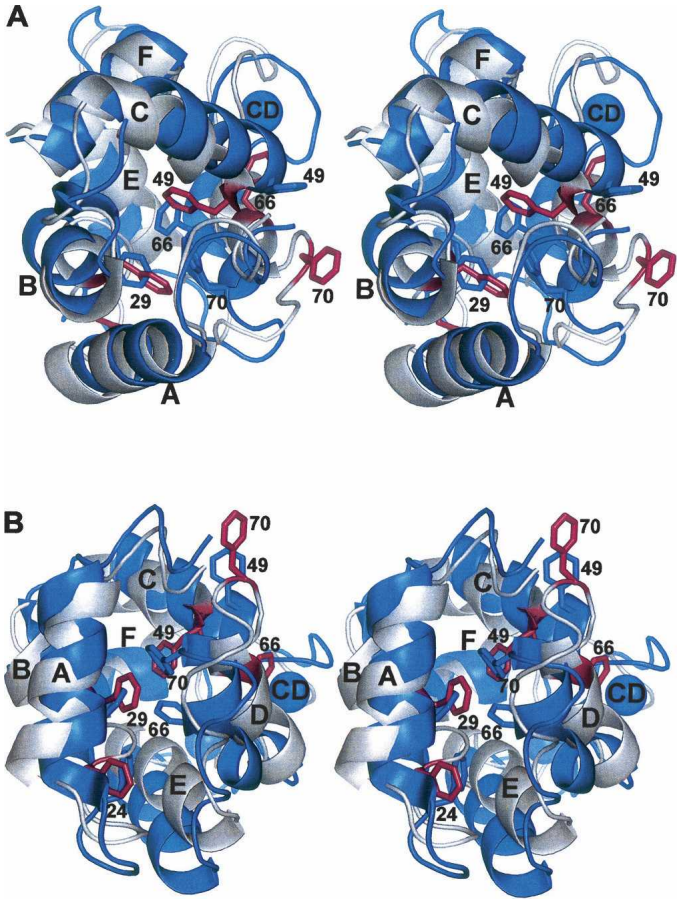

Figure 3. Stereoviews of the superimposed structures of Ca^{2+}-free (silver) and Ca^{2+}-bound (blue) rat β-PV. The two structures were superimposed so as to minimize the RMSD of the AB domain. The view in panel *B* represents an approximate 90° rotation about the horizontal axis of the view in panel *A*. Select phenylalanine side chains have been colored blue in the Ca^{2+}-loaded protein and magenta in the apo-protein. The coordinates for the Ca^{2+}-bound structure were obtained from a 1.3 Å crystal structure (PDB 1RRO) (Ahmed et al. 1993).

^{15}N relaxation data analysis

Relaxation data were collected on the Ca^{2+}-free protein at 20°C. The T_1 and T_2 data, acquired with the appropriate series of relaxation delays, display acceptable experimental uncertainties and are well accommodated by a two-parameter exponential decay model. Representative results are displayed in Supplemental Figure S4. R_1 and R_2 values were determined for 92 of 105 amide vectors. They are plotted in Figure 7A,B, respectively, and listed in Supplemental Table S2.

The overall rotational correlation time (τ_c) was estimated from a subset of the amide vectors (Fig. 7C, ●), those exhibiting an R_2/R_1 ratio within one standard deviation of the mean. Presumably, their relaxation behavior is largely determined by the overall tumbling of the molecule, with little influence from internal motions. These data are well accommodated by a spherically symmetric rotational diffusion model, yielding a rotational correlation time of 6.96 ± 0.04 ns. Axially symmetric and fully symmetric models yielded insignificant reductions in χ^2.

The $\{^1H\}^{15}N$ NOE values (Fig. 7D) exhibit a high degree of uniformity. Significant reductions in the NOE, indicating motion on a nanosecond timescale, are confined to residues 52, 60, and 61 in the CD loop, residues 91–96 in the EF loop, and the extreme C terminus. Excluding these outliers, the average NOE value is 0.81.

Internal mobility and model-free analysis

The Lipari–Szabo model-free formalism was used to examine main-chain flexibility in Ca^{2+}-free rat β-PV. Relaxation data for 92 amide vectors were included in the analysis, employing a spherically symmetric diffusion model. The results are displayed in Figure 7E,F, and the model-free parameters are listed in Supplemental Table S3.

The majority of signals (62/92) can be modeled with the overall rotational correlation time (τ_c) and a generalized order parameter (S^2) (Model 1). Eleven amide vectors

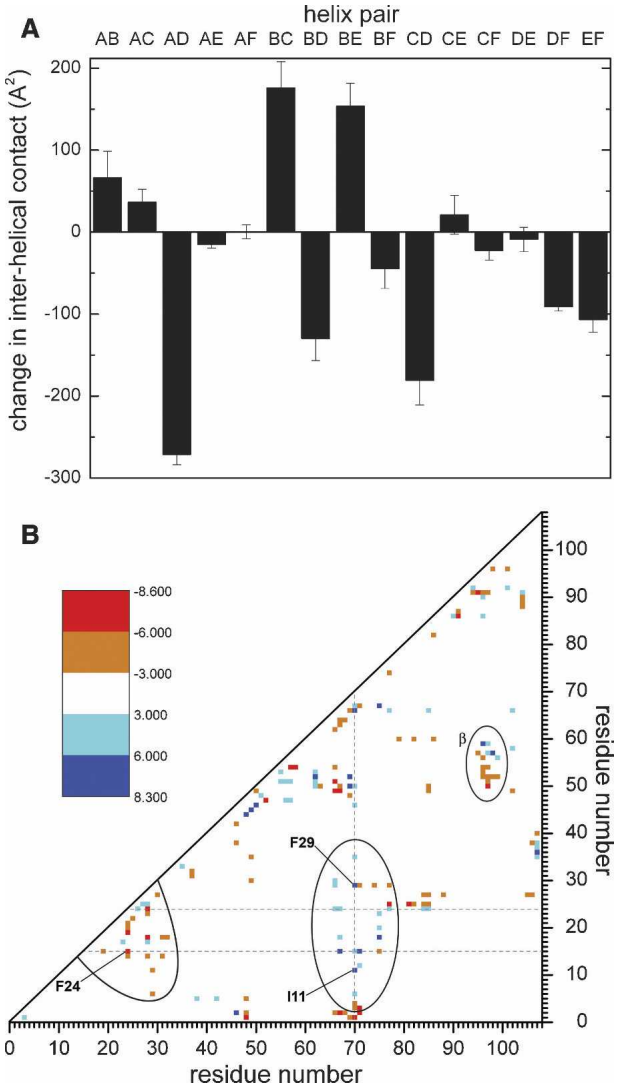

Figure 4. (*A*) Interhelical contacts in the Ca^{2+}-free and Ca^{2+}-bound forms of rat β-PV. The change in interhelical contact area that accompanies the removal of Ca^{2+} is plotted for each of the helix pairs. (*B*) Difference contact matrix. Orange/red symbols represent residue pairs with significantly increased contact in the apo-protein; cyan/blue symbols represent residue pairs with decreased contact in the apo-protein. For clarity, only differences that exceed the variance by at least a factor of three are shown. Details of the calculations are provided in Materials and Methods.

require a τ_e term to describe internal motion on the 20 ps–10 ns timescale. An additional 15 require an R_{ex} term to describe internal motion on the microsecond–millisecond timescale. (In this context, one reviewer noted that, due to the high CPMG field strength typically employed in R_2 measurements, the Lipari–Szabo analysis may fail to detect motion on the millisecond timescale.) Two amides (residues 52 and 96) can be accommodated only by inclusion of both τ_e and R_{ex} terms. Finally, two NH vectors (D94, G95) exhibit behavior consistent with motion on two timescales shorter than the overall rotational correlation time. Except for T3, A40, S41, F70, S71, and S77, all of the amide vectors incompatible with Model 1 reside in the CD and EF loops or at the C terminus. The relaxation behavior of the I2 vector was not reproduced by any of the models.

Discussion

Whereas typical parvalbumin CD and EF sites behave equivalently in titrations with divalent ions, the binding sites in rat β-PV are conspicuously nonequivalent. The Ca^{2+}- and Mg^{2+}-binding constants for the EF site, 2.5×10^7 and 9.0×10^3 M^{-1}, approach those of the rat α isoform (1.2×10^8 and 1.8×10^4 M^{-1}, respectively). By

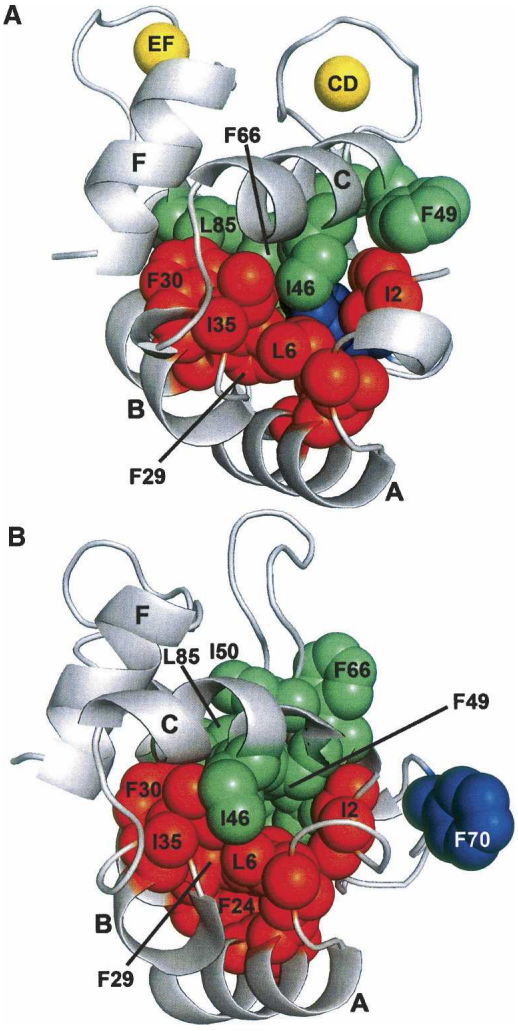

Figure 5. Ca^{2+} removal provokes rearrangement of the hydrophobic core. (*A*) In the Ca^{2+}-bound protein, F70 is deeply buried in the protein interior, intimately associated with apolar side chains from the AB domain. (*B*) In the Ca^{2+}-free state, F70 has withdrawn from the core, and the interactions between F70 and the AB domain have been broken. I46, F49, I50, F66, and L85 have also experienced significant displacements.

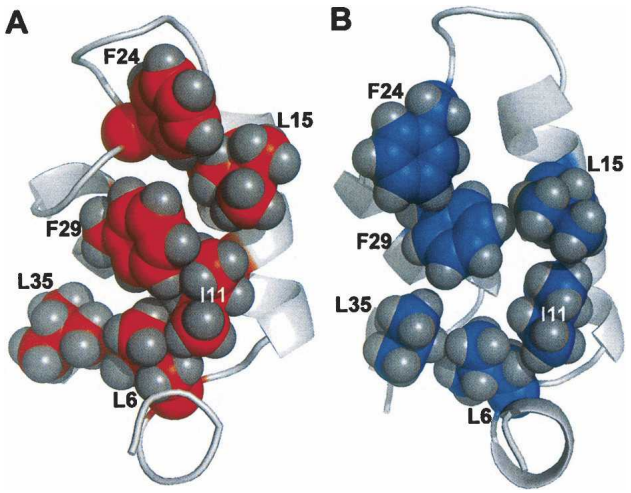

Figure 6. Ca^{2+} removal modifies hydrophobic contacts in the AB domain. The conformations of residues 6, 11, 15, 24, 29, and 35 are displayed for the Ca^{2+}-free (*A*) and Ca^{2+}-bound (*B*) states of the protein. The interactions between F24 and L15, F29 and I11, and L35 and L6 in the apo-protein are either less pronounced or absent in the presence of Ca^{2+}.

contrast, the CD site exhibits sharply attenuated divalent ion affinity, with Ca^{2+}- and Mg^{2+}-binding constants of 1.5×10^6 and 1.6×10^2 M^{-1} (Hapak et al. 1989; Cox et al. 1990; Henzl et al. 2004b).

The CD loop in rat β-PV differs from the PV consensus at residues 57–59, with Tyr-Leu-Asp replacing the otherwise invariant Phe-Ile-Glu sequence triad. However, divalent ion-binding behavior is relatively insensitive to mutations at these positions (Golden et al. 1989; Hapak et al. 1989; Palmisano et al. 1990; Trevino et al. 1991; Pauls et al. 1996b), suggesting that remote structural determinants contribute to the atypical divalent ion-binding signature of the CD site.

We recently replaced residues 49, 50, 57, 58, 59, and 60 with the corresponding residues from chicken parvalbumin 3 (CPV3). Although the resulting CD site is identical to that in CPV3 at 27 of 30 positions, the Ca^{2+} and Mg^{2+} affinities remain 1.5 and 2.9 kcal/mol, respectively, less favorable than those displayed by CPV3 (Henzl and Ndubuka 2006). This result further attests to the influence of structural features beyond the binding site.

Several years ago, ^{15}N relaxation data were collected on Ca^{2+}-free and -bound rat β-PV at 37°C (Henzl et al. 2002). Due to substantial exchange broadening at that temperature, it was possible to assign just 60 of the amide signals in the apo-protein. Interestingly, however, for the majority of N-H vectors in the AB and D/E regions, the order parameters were larger in the Ca^{2+}-free state. Apparently, Ca^{2+} removal decreases flexibility in these regions of the molecule, an indication that they may influence divalent ion-binding behavior.

To assess the potential impact of the AB domain, we studied association of the isolated AB and CD/EF domains from rat α- and β-PV (Henzl et al. 2004a). The interactions, homologous and heterologous, were characterized in two ways: Complex formation was examined in the presence of saturating Ca^{2+}, and the apparent Ca^{2+} affinity of each complex was examined by titrating an equimolar mixture of the AB and CD-EF fragments. Although the AB fragments from the α and β

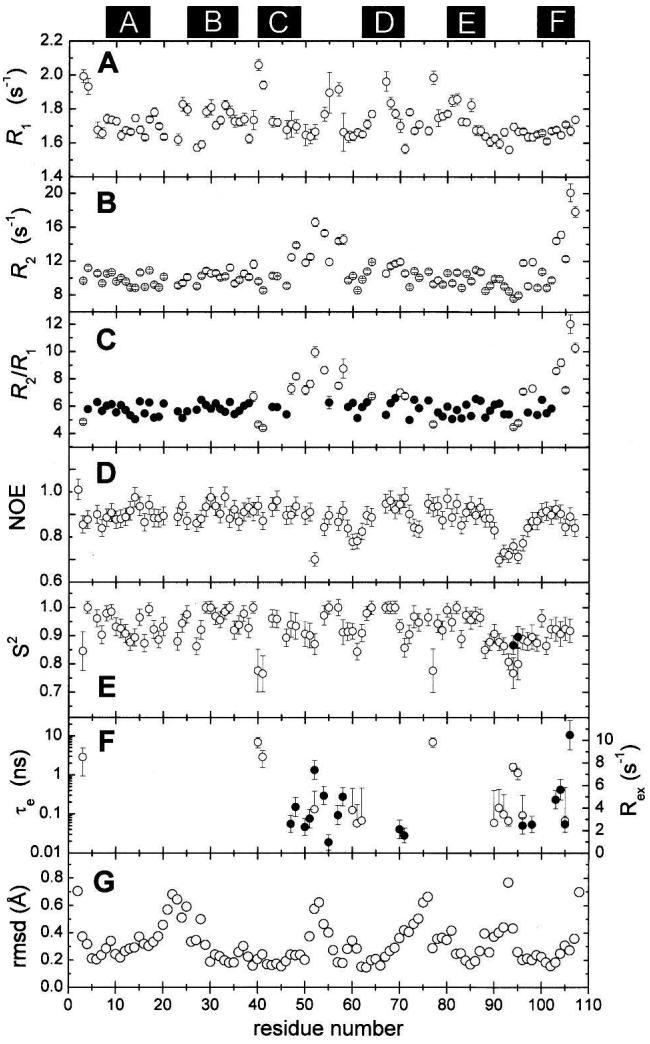

Figure 7. Summary of ^{15}N relaxation data and internal mobility analysis. (*A*) Experimental R_1 values. (*B*) Experimental R_2 values. (*C*) R_2/R_1 ratios. Filled circles (●) denote amide vectors included in the calculation of the mean value. (*D*) Experimental $\{^1H\}^{15}N$ NOE values. (*E*) Generalized order parameter (S^2) determined by model-free analysis, as described in the text. D94 and G95 required inclusion of a second order parameter (●), corresponding to motion on a slower timescale, to satisfactorily reproduce their relaxation behavior. (*F*) τ_e (○) and R_{ex} (●) values for those residues displaying motion on a timescale exceeding 20 ps. The locations of the six helical elements are indicated at the *top* of the figure. (*G*) Average RMSD for the backbone atom positions for each residue in the ensemble.

isoforms differ at 18 of 37 residues, the β CD-EF fragment exhibits higher affinity for the α AB fragment. Moreover, the resulting heterologous αβ complex displays substantially greater Ca^{2+} affinity. The apparent 2.3 kcal/mol improvement in free energy reflects a more favorable binding enthalpy and less favorable binding entropy.

The improved enthalpic term implies that, relative to β AB, the α AB fragment more readily assumes the conformation required for association with the CD-EF domain. The less favorable entropic term, on the other hand, implies that the isolated α AB fragment is relatively unstructured. Parenthetically, we had intended to produce both AB peptides as fusion proteins. Although successful for β AB, the α AB peptide thus obtained was invariably proteolyzed, necessitating its chemical synthesis. This observation suggests that the AB fragment from rat β-PV, but not from rat α-PV, adopts an ordered, protease-resistant structure in solution.

On the basis of these findings, it was suggested (1) that the β-PV AB domain has an intrinsic structural preference, which it manifests in the unliganded state, and (2) that the attenuated divalent ion affinity of rat β-PV reflects an energetic penalty attendant to placing the AB domain in its liganded conformation. Consistent with these ideas, this study finds that the interface between the AB and CD-EF domains differs significantly in the apo- and Ca^{2+}-bound proteins.

The relative positions of helices A, B, and F are little changed by Ca^{2+} removal (Fig. 3). However, the C, D, and E helices experience significant displacement. Their reorientation substantially alters intramolecular contacts. These changes can be readily appreciated, either at the level of entire helices (Fig. 4A) or at the level of individual residues (Fig. 4B). The altered contacts reflect a major reorganization of the hydrophobic core. The withdrawal of F70 and F66 from the protein interior provides the most tangible evidence of this reorganization. However, the side chains of I46, F49, I50, and L85 have also undergone repositioning.

This reshuffling of the apolar side chains results in remodeling of the AB/CD-EF interface. In the Ca^{2+}-loaded protein, residues I2, L6, I11, L15, and F29 make extensive contact with F70, in effect anchoring the C-terminal end of the D helix to the AB domain. These interactions are abolished when F70 vacates the hydrophobic core. Interactions between F66 and L67 and the AB domain are likewise diminished in the Ca^{2+}-free state. Liberated from their interdomain contacts, residues 6, 11, 15, 24, 29, and 35 instead form a network of intradomain hydrophobic interactions (Fig. 6).

Contact between the D helix and the A and B helices is sharply decreased in the apo-protein, largely accounting for the 9% reduction in apolar surface area buried at the AB/CD-EF interface. By contrast, F49 and L85 assume more interior positions in the Ca^{2+}-free state, contributing to a significant increase in contact between helix B and the C and E helices.

^{15}N relaxation data suggest that the peptide backbone remains rigid, on the picosecond–nanosecond timescale, in the apo-protein. In the previous ^{15}N relaxation study conducted on Ca^{2+}-free rat β-PV at 37°C (Henzl et al. 2002), the average order parameter (for those 60 residues that were assignable) was 0.90. The magnitude of the order parameter is expected to increase with decreasing temperature (Bracken et al. 1999). In accordance with prediction, the relaxation data presented here, collected at 20°C, yield an average S^2 value of 0.92.

In the present study, two-thirds of the amide vectors show no evidence for internal mobility on timescales exceeding 20 ps. Of the remaining vectors, 11 show evidence for motion on the nanosecond timescale, 15 show evidence for motion on the microsecond timescale, and a handful show evidence of more complex internal motions. With few exceptions, all of these reside within the CD and EF ion-binding loops (see below).

Model-free analysis returned S^2 values of 1.0 for nine amides. Significantly, four of these (K64, L67, Q68, K69) reside in the D helix, which, as noted above, undergoes a major transformation upon Ca^{2+} removal. Signal degeneracy prevented analysis of the vectors associated with Y65 and F66. The implication, however, is that straightening of the D helix is accompanied by significant rigidification. Residues 4, 34, 39, 77, and 82 also exhibit S^2 values of 1.0. Rat β-PV exhibits no tendency to dimerize in either the apo- or Ca^{2+}-bound forms (Henzl et al. 2002). Thus, the extreme S^2 values are not a consequence of self-association (Schurr et al. 1994; Baryshnikova and Sykes 2006).

Removal of Ca^{2+} might be expected to produce increased disorder within the CD and EF binding loops. However, the RMSDs within the binding loops are no more pronounced than those observed in the loops joining either the A and B helices or the D and E helices (Fig. 7G). This minimal conformational heterogeneity could be a reflection of Na^+ binding. Solvent cations can occupy vacant parvalbumin EF-hand motifs (Permyakov et al. 1983; Henzl et al. 2000). At a Na^+ concentration of 0.24 M, rat β-PV binds approximately two equivalents of the monovalent ion, with an estimated average binding constant of 60 M^{-1} (Henzl et al. 2000). Under the conditions employed for NMR data collection (170 mM Na^+, 4 mM protein), the binding loops would be ~90% occupied by the monovalent ion.

Although the binding loops exhibit little structural heterogeneity, the ^{15}N relaxation data suggest that residues in the loops, and nearby, are subject to motion on longer timescales. With respect to the CD loop (residues 51–62),

significantly elevated R_2/R_1 values are observed for F47, R48, I50, D51, N52, Q54, Y57, and L58. All of these residues, and S55 as well, require an R_{ex} term for satisfactory Lipari–Szabo modeling. These findings are indicative of motion on the microsecond timescale. N52, G60, D61, and E62 exhibit reduced $\{^1H\}^{15}N$ NOE values and require τ_e values to model internal mobility—suggestive of motion on the nanosecond timescale.

The EF loop displays less evidence for microsecond motion. There is no comparable elevation of R_2/R_1 values, and only K96 and I97 require the R_{ex} term. However, the EF loop residues apparently experience substantial motion on the nanosecond timescale. N91, D92, G93, D94, G95, and K96 exhibit markedly reduced $\{^1H\}^{15}N$ NOEs. These same residues, plus D90, require τ_e in the Lipari–Szabo analysis.

The structural data for rat β-PV were collected in buffered saline because detailed divalent ion-binding studies have been conducted under comparable solution conditions. The identity of the major solvent cation can significantly influence PV divalent ion-binding behavior. Ca^{2+}-free rat α-PV, for example, binds one equivalent of Na^+ but has negligible affinity for K^+. As a consequence, the average Ca^{2+}-binding constant increases from 1.2×10^8 M^{-1} in Na^+ solution to 1.4×10^9 M^{-1} in K^+ solution ($\Delta\Delta G_{tot}=-2.6$ kcal/mol) (Henzl et al. 2004b). Monovalent ion identity has a smaller impact on rat β-PV ($\Delta\Delta G_{tot}=-0.7$ kcal/mol), presumably because the apo-protein is capable of binding either Na^+ or K^+ (Henzl et al. 2000, 2004b). Although the binding stoichiometries are not identical for the two ions, it is anticipated that the solution structure of rat β-PV in 150 mM K^+ would closely resemble the structure described here.

Under resting-state conditions in the cell (pCa = −7, pMg = −3), the predominant form of rat β-PV is predicted to have Mg^{2+} bound in the EF site and K^+ bound at the CD site. The divalent ion-free form of the protein studied here is negligibly populated under physiological conditions. However, ligand affinity reflects the difference in the free energies of the bound and ligand-free states. Thus, the unliganded protein influences binding energetics regardless of the extent to which it is populated in vivo.

The Ca^{2+}-bound structures of rat α- and β-PV are remarkably similar (Ahmed et al. 1993; McPhalen et al. 1994; Bottoms et al. 2004). The RMSD for their superimposed polypeptide backbones is just 0.8–0.9 Å. Inspection of the Ca^{2+}-loaded molecules offers little insight into the source of the apparent 5.5 kcal/mol difference in standard binding free energy observed in 0.15 M KCl at pH 7.4. This discrepancy could merely reflect multiple, minor structural and energetic differences in the metal ion-bound forms. Alternatively, the divergent divalent ion-binding behavior could be dictated at the level of the apo-proteins. In principle, ligand affinity can be modulated by adjusting the stability of the apo-form, with stabilization producing a reduction in affinity.

This study suggests that Ca^{2+}-free rat β-PV adopts a conformation distinct from that of the Ca^{2+}-bound state. Rearrangement of the C, D, and E helices has substantively altered the relative orientation of the AB and CD-EF domains. Because divalent ion binding requires their reversal, structural alterations of the magnitude described here could compromise binding affinity. Moreover, consistent with the divalent ion-binding signature of the protein, the observed differences are predicted to exert their primary effect on the CD site. Because Ca^{2+} removal has a more modest impact on the E and F helices, the energetic penalty associated with converting the EF site to its bound configuration should be substantially smaller than that associated with isomerizing the CD site.

In conclusion, these findings suggest that the unusual divalent ion-binding behavior of rat β-PV may be strongly influenced by the structural preferences of the apo-protein. If correct, the Ca^{2+}-free state of a more typical PV isoform should more closely resemble that of the Ca^{2+}-loaded state. It will be interesting to learn whether the structure of Ca^{2+}-free rat β-PV differs substantively from the apo-PV norm.

Materials and Methods

Materials

Celtone was obtained from Spectra Stable Isotopes. Pf1 bacteriophage were ordered from ASLA BIOTECH Ltd. All other common chemicals and reagents were obtained from Sigma-Aldrich or Fisher Scientific Co.

Protein expression and purification

Recombinant rat β-PV was expressed and purified as described previously (Hapak et al. 1989). Besides $^{13}C_6$-d-glucose and/or $^{15}NH_4Cl$, the medium consisted of M9 salts supplemented with 2.5% (v/v) Celtone, 100 μM $FeCl_3$, trace elements, and ampicillin (300 μg/mL). Each liter yielded 20–25 mg of protein, with purity exceeding 98%.

NMR sample preparation

Sufficient protein to yield a 4 mM sample was concentrated to 5 mL by ultrafiltration, then dialyzed at 4°C for 48 h, against 4 L of 0.15 M NaCl, 0.025 M HEPES, 5.0 mM EDTA (pH 7.4). Dialysis was continued for 48 h against 0.15 M NaCl, 0.01 M Mes, 5.0 mM EDTA (pH 6.0). After adding 0.1 volume of buffer prepared in D_2O, as well as sodium azide (final concentration 0.1%), the solution was concentrated to 0.35 mL and loaded into a 5-mm Shigemi microcell (Shigemi, Inc.).

For measurement of residual dipolar couplings, partial alignment was achieved by addition of Pf1 bacteriophage. Prior to combining the phage with the protein, it was dialyzed against

0.15 M NaCl, 0.025 M Mes, 5.0 mM EDTA (pH 6.0). The phage concentration in the resulting sample was estimated at 13 mg/mL, based on an observed 14-Hz splitting of the HOD signal.

NMR spectroscopy

All data were acquired at 20°C with BioPack pulse sequences on a Varian INOVA 600-MHz spectrometer, employing a triple-resonance cryoprobe equipped with pulsed-field *z* gradient. ^{1}H chemical shifts were referenced relative to DSS; ^{13}C and ^{15}N shifts were referenced indirectly, employing the $^{1}H/X$ frequency ratios. Data were processed with NMRPipe and analyzed with Sparky (T.D. Goddard and D.G. Kneller, University of California, San Francisco).

Resonance assignments

Backbone resonance assignments were made using the following pairs of 3D experiments: HNCA (Ikura et al. 1990) and HN(CO)CA (Bax and Ikura 1991); HNCACB (Kay et al. 1994; Muhandiram and Kay 1994) and CBCA(CO)NH (Grzesiek and Bax 1992); and HNCO (Ikura et al. 1990) and HCACOCANH (Lohr and Ruterjans 2005). Aliphatic ^{13}C assignments beyond C^{β} were collected using the CCONH (Grzesiek et al. 1993) spectrum. Aliphatic side-chain ^{1}H assignments were made with HCCONH (Grzesiek et al. 1993), ^{15}N-edited TOCSY-HSQC (Marion et al. 1989a), and HCCH-TOCSY (Kay et al. 1993) experiments. Two-dimensional HBCBCGCDHD (Yamazaki et al. 1993) and HBCBCGCDCEHE (Yamazaki et al. 1993) spectra provided assignments for the aromatic protons. Stereospecific assignments of the methyl protons in valine and leucine were made by analysis of a fractionally ^{13}C-labeled sample (Neri et al. 1989). Asparagine and glutamine side-chain amides were assigned by matching the α/β (Asn) or β/γ (Gln) carbon shifts in the CBCACONH spectrum with the amide signals.

Structural restraints

For collection of NOE-based distance restraints, a 3D ^{15}N-edited NOESY-HSQC (Marion et al. 1989b) data set was collected on ^{15}N-labeled protein, employing a mixing time of 125 ms. A corresponding ^{13}C-edited experiment was performed on $^{13}C,^{15}N$-labeled material, using a mixing time of 100 ms. Cross peaks were picked manually and integrated in Sparky.

ϕ,ψ dihedral angle restraints were obtained from TALOS (Cornilescu et al. 1999) and CSI (Wishart and Sykes 1994). In addition, a 3D HNHA experiment (Vuister and Bax 1993) was conducted on ^{15}N-labeled protein, and the magnitude of $J_{HNH\alpha}$ was used to constrain the ϕ angle.

For the estimation of ^{1}H-^{15}N RDCs, ^{1}H-^{15}N splittings were measured on unaligned and partially aligned samples using the ^{1}H-^{15}N HSQC-IPAP pulse sequence (Ottiger et al. 1998). Peak positions were automatically picked in Sparky. Subtraction of the unaligned splitting from that observed in the aligned sample yielded the value of the ^{1}H-^{15}N RDC.

^{15}N relaxation data were collected on ^{15}N-labeled protein, employing the T_1, T_2, and $\{^{1}H\}^{15}N$ NOE pulse sequences supplied in BioPack. R_1 data were acquired with relaxation delays of 50, 100, 150, 250, 350, 450, 600, 800, 1000, and 1200 ms. R_2 data were acquired with delays of 10, 30, 50, 70, 90, 110, 130, 150, 170, and 190 ms. Replicate data were obtained at three delay values for evaluation of experimental uncertainty. For the measurement of steady-state heteronuclear {1H}15N-NOEs, HSQC spectra were collected, with or without proton saturation (3.0 sec), employing a total recycle delay period of 5.0 sec. Duplicate experiments were performed to obtain an estimate of the experimental uncertainty.

Structure calculations were performed with ARIA2.0a (Habeck et al. 2004). ARIA (ambiguous restraints for iterative assignment) integrates automated NOE assignments with CNS-based structure calculations (Linge et al. 2001). Supplied with chemical shift assignments and one or more NOE lists, ARIA produces a set of calibrated ambiguous distance restraints (ADRs). These serve as the input for CNS (Brunger et al. 1998) calculations, together with any additional structural restraints. The resulting set of lowest energy structures is used to modify the ADR list. The initial ambiguous restraint list is generated with the assumption of an extended polypeptide chain and a large violation tolerance, e.g., 1000 Å. Under these conditions, there is no discrimination between potential contributions to an ambiguous NOE cross peak, and only unambiguous NOEs influence the structure determination. In subsequent iterations, however, the violation tolerance is reduced, finally to 0.1 Å. As this tolerance shrinks, certain potential assignments are eliminated—reducing the degree of ambiguity associated with a particular cross peak and, in favorable cases, producing unambiguous restraints.

Initial structure calculations included a fairly extensive set of manual ^{1}H-^{1}H NOE assignments (350 total). During the review process, however, it was pointed out that these manual assignments are interpreted as unambiguous restraints by ARIA and can strongly influence the trajectory of the calculation. Thus, the calculations were repeated, omitting manual crosspeak assignments. Besides the ^{15}N- and ^{13}C-edited NOESY peak lists, the initial input included dihedral angle restraints (TALOS, CSI, and estimates of ϕ derived from $^{3}J_{HNH\alpha}$ values), and ^{1}H-^{15}N RDC restraints. Preliminary estimates for the rhombicity (R) and magnitude (D_a) of the alignment tensor—0.66 and −13.9 Hz, respectively—were obtained from a histogram analysis using EHM (Bryce and Bax 2004). After each round of calculation, the lowest energy structure was examined with PALES (Zweckstetter and Bax 2000) to obtain improved estimates of D_a and R. The lowest ARIA energies and minimal SANI violations were obtained with values of −10.7 Hz and 0.59, respectively.

The quality of the final structures was analyzed using PROCHECK (Laskowski et al. 1993). The area of contact between the AB and CD-EF domains in the Ca^{2+}-free state was estimated for each structure in the ensemble using the surface command of CNS, employing a probe radius of 1.4 Å. The interdomain contact area was defined as the sum of the solvent-accessible surface areas of the individual, isolated domains minus the accessible area of the entire protein. Hydrogen atoms were included in the calculations. Similar calculations were performed on the crystal structure of Ca^{2+}-bound rat β-PV (PDB 1RRO), after adding hydrogen atoms. The mean and standard deviation are reported for the NMR-derived structures.

To compare the extent of interhelical contact in the apo- and Ca^{2+}-bound states, we first summed the surface areas of the individual helices in a given helix pair. We then determined the surface area for that pair, in isolation, as oriented in the protein. The difference between these two values provided an estimate of the interhelical contact. These calculations were performed on the Ca^{2+}-bound crystal structure and each conformer of the Ca^{2+}-free ensemble. The mean and standard deviation for the latter are reported in Supplemental Table S1.

Data for the difference contact matrix in Figure 4B were calculated as follows. First, the interresidue contact area for

each pair of residues in a given structure was calculated as the sum of the solvent-accessible surface areas of the individual, isolated residues minus the surface area of the pair, as oriented in the protein. This procedure generated 5778 interresidue contact surface area values per structure. For the apo-protein, the interresidue contact values were averaged over the 20 models in the ensemble. These ensemble-averaged values were then subtracted from the corresponding values for the Ca^{2+}-bound structure to generate 5778 difference-contact-area values. These values were then scaled so as to yield an average value of zero and a variance of 1.0.

^{15}N relaxation analysis

Peak intensities in the T_1, T_2, and $\{^1H\}^{15}N$ NOE data sets were measured automatically in Sparky. R_1 and R_2 values were extracted for each peak by fitting the signal intensities to a two-parameter single-exponential decay, in Origin, version 7.5 (OriginLab). The NOE values represent the ratio of the signal intensities in the presence and absence of proton saturation. These relaxation data were analyzed with Tensor2 (Dosset et al. 2000).

The overall rotational correlation time (τ_c) was obtained using data for a subset of the amide vectors having R_2/R_1 values falling within one standard deviation of the mean value (Tjandra et al. 1995). Obvious outliers were excluded from the calculation of the mean. The isotropic rotational diffusion model yielded a τ_c value of 6.96 ± 0.04 ns, which corresponds to a rotational diffusion coefficient of 2.40×10^7 sec^{-1}. The axially symmetric model yielded two minima. In one case, the $D_{\|}$ and $D_{\perp}$ values were 2.44×10^7 sec^{-1} and 2.26×10^7 sec^{-1}, respectively ($D_{\|}/D_{\perp} = 1.08$). In the other, $D_{\|}$ and $D_{\perp}$ were 2.32×10^7 sec^{-1} and 2.52×10^7 sec^{-1} ($D_{\|}/D_{\perp} = 0.92$). The fully anisotropic model yielded D_x, D_y, and D_z values of 2.26×10^8 sec^{-1}, 2.42×10^8 sec^{-1}, and 2.46×10^8 sec^{-1}. Neither asymmetric model afforded a significant decrease in χ^2.

Internal mobilities were examined using the Lipari–Szabo model-free formalism (Lipari and Szabo 1982a,b). Tensor2 employs the five models suggested by Clore et al. (1990a,b) and the model selection strategy described by Mandel et al. (1995). Model 1 assumes that any internal motions are very rapid, with relaxation of the amide vector in question dictated by overall tumbling and a generalized order parameter, S^2. Model 2 includes an internal correlation time (τ_e), in addition to S^2, to allow for motion on the nanosecond timescale. Model 3 includes S^2 and R_{ex}, a rate constant that describes microsecond–millisecond motion. Model 4 includes S^2, τ_e, and R_{ex}. Model 5 is reserved for NH vectors having internal motions on two timescales shorter than the overall correlation time. It includes two order parameters—S_f^2 for rapid motion ($\leq$ 20 ps) and S_s^2 for slower motion (20–500 ps). The five models are tested iteratively, in order of increasing complexity, until the data are adequately reproduced by Monte Carlo simulation.

Coordinate and data deposition

The atomic coordinates and structural restraints have been deposited in the Protein Data Bank (PDB 2NLN). ^1H, ^{15}N, and ^{13}C assignments have been deposited in BioMagResBank (BMRB 7322).

Electronic supplemental material

Supplemental material for this article includes a comparison of the ^1H,^{15}N-HSQC spectra of apo- and Ca^{2+}-bound rat β-PV (Supplemental Fig. S1), a depiction of the sequential C^α and C^β connectivities between residues 32–41 of Ca^{2+}-free rat β-PV (Supplemental Fig. S2), the sequential distribution of NMR restraints used in the calculation (Supplemental Fig. S3), and representative ^{15}N relaxation data (R_1, R_2) with corresponding least-squares fits (Supplemental Fig. S4). Supplemental Table S1 contains the numerical estimates of interhelical contact in apo- and Ca^{2+}-bound β-PV. Supplemental Table S2 lists the R_1, R_2, and NOE values measured for Ca^{2+}-free rat β-PV. Supplemental Table S3 lists the Lipari–Szabo model-free parameters obtained by fitting the R_1, R_2, and NOE data.

Acknowledgments

The authors thank Dr. Wei Wycoff, staff NMR Spectroscopist for the MU NMR Facility, for her valuable assistance with the acquisition of the NMR data described herein. Matt Stanley, Systems Administrator Expert, is acknowledged for his outstanding technical support of the Linux-based machines in the Biochemistry Department and MU Structural Biology Core Facility. This work was supported by NSF awards MCB0131166 and MCB0543476 (to M.T.H. and J.J.T.).

References

Ahmed, F.R., Rose, D.R., Evans, S.V., Pippy, M.E., and To, R. 1993. Refinement of recombinant oncomodulin at 1.30 Å resolution. *J. Mol. Biol.* **230:** 1216–1224.

Babini, E., Bertini, I., Capozzi, F., Del Bianco, C., Hollender, D., Kiss, O.T., Luchinat, C., and Quattrone, A. 2004. Solution structure of human β-parvalbumin and structural comparison with its paralog α-parvalbumin and with their rat orthologs. *Biochemistry* **43:** 16076–16085.

Baig, I., Bertini, I., Del Bianco, C., Gupta, Y.K., Lee, Y.-M., Luchinat, C., and Quattrone, A. 2004. Paramagnetism-based refinement strategy for the solution structure of human α-parvalbumin. *Biochemistry* **43:** 5562–5573.

Baryshnikova, O.K. and Sykes, B.D. 2006. Backbone dynamics of SDF-1α determined by NMR: Interpretation in the presence of monomer-dimer equilibrium. *Protein Sci.* **15:** 2568–2578.

Bax, A. and Ikura, M. 1991. An efficient 3D NMR technique for correlating the proton and 15N backbone amide resonances with the α-carbon of the preceding residue in uniformly 15N/13C enriched proteins. *J. Biomol. NMR* **1:** 99–104.

Berchtold, M.W. and Means, A.R. 1985. The Ca^{2+}-binding protein parvalbumin: Molecular cloning and developmental regulation of mRNA abundance. *Proc. Natl. Acad. Sci.* **82:** 1414–1418.

Berridge, M.J. 2004. Calcium signal transduction and cellular control mechanisms. *Biochim. Biophys. Acta* **1742:** 3–7.

Berridge, M.J. 2005. Unlocking the secrets of cell signaling. *Annu. Rev. Physiol.* **67:** 1–21.

Berridge, M.J., Bootman, M.D., and Roderick, H.L. 2003. Calcium signalling: Dynamics, homeostasis and remodelling. *Nat. Rev. Mol. Cell Biol.* **4:** 517–529.

Bottoms, C.A., Schuermann, J.P., Agah, S., Henzl, M.T., and Tanner, J.J. 2004. Crystal structure of rat α-parvalbumin at 1.05 Å resolution. *Protein Sci.* **13:** 1724–1734.

Bracken, C., Carr, P.A., Cavanagh, J., and Palmer III, A.G. 1999. Temperature dependence of intramolecular dynamics of the basic leucine zipper of GCN4: Implications for the entropy association with DNA. *J. Mol. Biol.* **285:** 2133–2146.

Brunger, A.T., Adams, P.D., Clore, G.M., DeLano, W.L., Gros, P., Grosse-Kunstleve, R.W., Jiang, J.S., Kuszewski, J., Nilges, M., Pannu, N.S., et al. 1998. Crystallography and NMR System: A new software suite for macromolecular structure determination. *Acta Crystallogr. D Biol. Crystallogr.* **54:** 905–921.

Bryce, D.L. and Bax, A. 2004. Application of correlated residual dipolar couplings to the determination of the molecular alignment tensor magnitude of oriented proteins and nucleic acids. *J. Biomol. NMR* **28:** 273–287.

Celio, M.R., Pauls, T., and Schwaller, B. 1996. *Guidebook to the calcium-binding proteins*. Oxford University Press, Oxford, UK.

Clayshulte, T.M., Taylor, D.F., and Henzl, M.T. 1990. Reactivity of cysteine 18 in oncomodulin. *J. Biol. Chem.* **265:** 1800–1805.

Clore, G.M., Driscoll, P.C., Wingfield, P.T., and Gronenborn, A.M. 1990a. Analysis of the backbone dynamics of interleukin-1β using two-dimensional inverse detected heteronuclear ^{15}N-^{1}H NMR spectroscopy. *Biochemistry* **29:** 7387–7401.

Clore, G.M., Szabo, A., Bax, A., Kay, L.E., Driscoll, P.C., and Gronenborn, A.M. 1990b. Deviations from the simple two-parameter model-free approach to the interpretation of nitrogen-15 nuclear magnetic relaxation of proteins. *J. Am. Chem. Soc.* **112:** 4989–4991.

Cornilescu, G., Delaglio, F., and Bax, A. 1999. Protein backbone angle restraints from searching a database for chemical shift and sequence homology. *J. Biomol. NMR* **13:** 289–302.

Cox, J.A., Milos, M., and MacManus, J.P. 1990. Calcium- and magnesium-binding properties of oncomodulin. Direct binding studies and microcalorimetry. *J. Biol. Chem.* **265:** 6633–6637.

DeLano, W.L. 2002. The PyMOL molecular graphics system. DeLano Scientific, San Carlos, CA.

Dosset, P., Hus, J.-C., Blackledge, M., and Marion, D. 2000. Efficient analysis of macromolecular rotational diffusion from heteronuclear relaxation data. *J. Biomol. NMR* **16:** 23–28.

Fohr, U.G., Weber, B.R., Muntener, M., Staudenmann, W., Hughes, G.J., Frutiger, S., Banville, D., Schafer, B.W., and Heizmann, C.W. 1993. Human α and β parvalbumins. Structure and tissue-specific expression. *Eur. J. Biochem.* **215:** 719–727.

Gillen, M.F., Banville, D., Rutledge, R.G., Narang, S., Seligy, V.L., Whitfield, J.F., and MacManus, J.P. 1987. A complete complementary DNA for the oncodevelopmental calcium-binding protein, oncomodulin. *J. Biol. Chem.* **262:** 5308–5312.

Golden, L.F., Corson, D.C., Sykes, B.D., Banville, D., and MacManus, J.P. 1989. Site-specific mutants of oncomodulin. ^{1}H NMR and optical stopped-flow studies of the effect on the metal binding properties of an Asp59-Glu59 substitution in the calcium-specific site. *J. Biol. Chem.* **264:** 20314–20319.

Goodman, M. and Pechere, J.F. 1977. The evolution of muscular parvalbumins investigated by the maximum parsimony method. *J. Mol. Evol.* **9:** 131–158.

Grzesiek, S. and Bax, A. 1992. Correlating backbone amide and side chain resonances in larger proteins by multiple relayed triple resonance NMR. *J. Am. Chem. Soc.* **114:** 6291–6293.

Grzesiek, S., Anglister, J., and Bax, A. 1993. Correlation of backbone amide and aliphatic side-chain resonances in 13C/15N-enriched proteins by isotropic mixing of carbon-13 magnetization. *J. Magn. Reson.* **101:** 114–119.

Habeck, M., Rieping, W., Linge, J.P., and Nilges, M. 2004. NOE assignment with ARIA 2.0: The nuts and bolts. *Methods Mol. Biol.* **278:** 379–402.

Hapak, R.C., Lammers, P.J., Palmisano, W.A., Birnbaum, E.R., and Henzl, M.T. 1989. Site-specific substitution of glutamate for aspartate at position 59 of rat oncomodulin. *J. Biol. Chem.* **264:** 18751–18760.

Heizmann, C.W. and Kagi, U. 1989. Structure and function of parvalbumin. *Adv. Ex. Med. Biol.* **255:** 215–222.

Henzl, M.T. and Ndubuka, K. 2006. Low-affinity signature of the rat β-parvalbumin CD site. Evidence for remote determinants. *Biochemistry* **46:** 23–35.

Henzl, M.T., Shibasaki, O., Comegys, T.H., Thalmann, I., and Thalmann, R. 1997. Oncomodulin is abundant in the organ of Corti. *Hear. Res.* **106:** 105–111.

Henzl, M.T., Larson, J.D., and Agah, S. 2000. Influence of monovalent cations on rat α- and β-parvalbumin stabilities. *Biochemistry* **39:** 5859–5867.

Henzl, M.T., Wycoff, W.G., Larson, J.D., and Likos, J.J. 2002. ^{15}N nuclear magnetic resonance relaxation studies on rat β-parvalbumin and the pentacarboxylate variants, S55D and G98D. *Protein Sci.* **11:** 158–173.

Henzl, M.T., Agah, S., and Larson, J.D. 2004a. Association of the AB and CD-EF domains from rat α- and β-parvalbumin. *Biochemistry* **43:** 10906–10917.

Henzl, M.T., Larson, J.D., and Agah, S. 2004b. Influence of monovalent cation identity on parvalbumin divalent ion-binding properties. *Biochemistry* **43:** 2747–2763.

Ikura, M., Kay, L.E., and Bax, A. 1990. A novel approach for sequential assignment of ^{1}H, ^{13}C, and ^{15}N spectra of larger proteins: Heteronuclear triple-resonance three-dimensional NMR spectroscopy. Application to calmodulin. *Biochemistry* **29:** 4659–4667.

Kawasaki, H. and Kretsinger, R.H. 1995. Calcium-binding proteins 1: EF-hands. *Protein Profile* **2:** 297–490.

Kay, L.E., Xu, G.Y., Singer, A.U., Muhandiram, D.R., and Forman-Kay, J.D. 1993. A gradient-enhanced HCCH-TOCSY experiment for recording side-chain proton and carbon-13 correlations in water samples of proteins. *J. Magn. Reson.* **B101:** 333–337.

Kay, L.E., Xu, G.Y., and Yamazaki, T. 1994. Enhanced-sensitivity triple-resonance spectroscopy with minimal H_2O saturation. *J. Magn. Reson.* **109:** 129–133.

Kretsinger, R.H. 1980. Structure and evolution of calcium-modulated proteins. *CRC Crit. Rev. Biochem.* **8:** 119–174.

Kretsinger, R.H. and Nockolds, C.E. 1973. Carp muscle calcium-binding protein. II. Structure determination and general description. *J. Biol. Chem.* **248:** 3313–3326.

Laskowski, R.A., MacArthur, M.W., Moss, D.S., and Thornton, J.M. 1993. PROCHECK: A program to check the stereochemical quality of protein structures. *J. Appl. Crystallogr.* **26:** 283–291.

Linge, J.P., O'Donoghue, S.I., and Nilges, M. 2001. Automated assignment of ambiguous nuclear Overhauser effects with ARIA. *Methods Enzymol.* **339:** 71–90.

Lipari, G. and Szabo, A. 1982a. Model-free approach to the interpretation of nuclear magnetic resonance relaxation in macromolecules. 1. Theory and range of validity. *J. Am. Chem. Soc.* **104:** 4546–4559.

Lipari, G. and Szabo, A. 1982b. Model-free approach to the interpretation of nuclear magnetic resonance relaxation in macromolecules. 2. Analysis of experimental results. *J. Am. Chem. Soc.* **104:** 4559–4570.

Lohr, F. and Ruterjans, H. 2005. A new triple-resonance experiment for the sequential assignment of backbone resonances in proteins. *J. Biomol. NMR* **6:** 189–197.

MacManus, J.P., Watson, D.C., and Yaguchi, M. 1983. The complete amino acid sequence of oncomodulin—A parvalbumin-like calcium-binding protein from Morris hepatoma 5123tc. *Eur. J. Biochem.* **136:** 9–17.

Mandel, A.M., Akke, M., and Palmer III, A.G. 1995. Backbone dynamics of *Escherichia coli* ribonuclease HI: Correlations with structure and function in an active enzyme. *J. Mol. Biol.* **246:** 144–163.

Marion, D., Driscoll, P.C., Kay, L.E., Wingfield, P.T., Bax, A., Gronenborn, A.M., and Clore, G.M. 1989a. Overcoming the overlap problem in the assignment of ^{1}H NMR spectra of larger proteins by use of three-dimensional heteronuclear ^{1}H-^{15}N Hartmann-Hahn-multiple quantum coherence and nuclear Overhauser-multiple quantum coherence spectroscopy: Application to interleukin 1β. *Biochemistry* **28:** 6150–6156.

Marion, D., Kay, L.E., Sparks, S.W., Torchia, D., and Bax, A. 1989b. Three-dimensional heteronuclear NMR of nitrogen-15 labeled proteins. *J. Am. Chem. Soc.* **111:** 1515–1517.

McPhalen, C.A., Sielecki, A.R., Santarsiero, B.D., and James, M.N.G. 1994. Refined crystal structure of rat parvalbumin, a mammalian α-lineage parvalbumin, at 2.0 Å resolution. *J. Mol. Biol.* **235:** 718–732.

Moncrief, N.D., Kretsinger, R.H., and Goodman, M. 1990. Evolution of EF-hand calcium-modulated proteins. I. Relationships based on amino acid sequences. *J. Mol. Evol.* **30:** 522–562.

Muhandiram, D.R. and Kay, L.E. 1994. Gradient-enhanced triple-resonance three-dimensional NMR experiments with improved sensitivity. *J. Magn. Reson.* **103:** 203–216.

Neri, D., Szyperski, T., Otting, G., Senn, H., and Wuytack, F. 1989. Stereospecific nuclear magnetic resonance assignments of the methyl groups of valine and leucine in the DNA-binding domain of the 434 repressor by biosynthetically directed fractional ^{13}C labeling. *Biochemistry* **28:** 7510–7516.

Ottiger, M., Delaglio, F., and Bax, A. 1998. Measurement of J and dipolar couplings from simplified two-dimensional NMR spectra. *J. Magn. Reson.* **131:** 373–378.

Palmisano, W.A., Trevino, C.L., and Henzl, M.T. 1990. Site-specific replacement of amino acid residues within the CD binding loop of rat oncomodulin. *J. Biol. Chem.* **265:** 14450–14456.

Pauls, T.L., Cox, J.A., and Berchtold, M.W. 1996a. The Ca^{2+}-binding proteins parvalbumin and oncomodulin and their genes: New structural and functional findings. *Biochim. Biophys. Acta* **1306:** 39–54.

Pauls, T.L., Durussel, I., Clark, I.D., Szabo, A.G., Berchtold, M.W., and Cox, J.A. 1996b. Site-specific replacement of amino acid residues in the CD site of rat parvalbumin changes the metal specificity of this Ca^{2+}/Mg^{2+}-mixed site toward a Ca^{2+}-specific site. *Eur. J. Biochem.* **242:** 249–255.

Permyakov, E.A., Kalinichenko, L.P., Medvedkin, V.N., Burstein, E.A., and Gerday, C. 1983. Sodium and potassium binding to parvalbumins measured by means of intrinsic protein fluorescence. *Biochim. Biophys. Acta* **749:** 185–191.

Sakaguchi, N., Henzl, M.T., Thalmann, I., Thalmann, R., and Schulte, B.A. 1998. Oncomodulin is expressed exclusively by outer hair cells in the organ of Corti. *J. Histochem. Cytochem.* **46:** 29–39.

Schurr, J.M., Babcock, H.P., and Fujimoto, B.S. 1994. A test of the model-free formulas. Effects of anisotropic rotational diffusion and dimerization. *J. Magn. Reson.* **B105:** 211–224.

Strynadka, N.C.J. and James, M.N.G. 1989. Crystal structures of the helix-loop-helix calcium-binding proteins. *Annu. Rev. Biochem.* **58:** 951–998.

Tjandra, N., Feller, S.E., Pastor, R.W., and Bax, A. 1995. Rotational diffusion anisotropy of human ubiquitin from 15N NMR relaxation. *J. Am. Chem. Soc.* **117:** 12562–12566.

Trevino, C.L., Boschi, J.M., and Henzl, M.T. 1991. Interactions between residues in the oncomodulin CD domain influence Ca^{2+} ion-binding affinity. *J. Biol. Chem.* **266:** 11301–11308.

Vuister, G.W. and Bax, A. 1993. Quantitative *J* correlation: A new approach for measuring homonuclear three-bond $J(H^NH^\alpha)$ coupling constants in ^{15}N-enriched proteins. *J. Am. Chem. Soc.* **115:** 7772–7777.

Wishart, D.S. and Sykes, B.D. 1994. The 13C chemical-shift index: A simple method for the identification of protein secondary structure using 13C chemical-shift data. *J. Biomol. NMR* **4:** 171–180.

Yamazaki, T., Forman-Kay, J.D., and Kay, L.E. 1993. Two-dimensional NMR experiments for correlating $^{13}C\beta$ and $^{1}H\delta/\varepsilon$ chemical shifts of aromatic residues in ^{13}C-labeled proteins via scalar couplings. *J. Am. Chem. Soc.* **115:** 11054–11055.

Yin, Y., Henzl, M.T., Lorber, B., Nakazawa, T., Thomas, T.T., Jiang, F., Langer, R., and Benowitz, L.I. 2006. Oncomodulin is a macrophage-derived signal for axon regeneration in retinal ganglion cells. *Nat. Neurosci.* **9:** 843–852.

Zweckstetter, M. and Bax, A. 2000. Prediction of sterically induced alignment in a dilute liquid crystalline phase: Aid to protein structure determination by NMR. *J. Am. Chem. Soc.* **122:** 3791–3792.